Origin of low-field microwave absorption in metallic magnetic films evidenced in FeRh/Ta/GaAs

Doan Ba Nguyen, Giovanni Olivetti, Timothée Tremblais, Isabella Boventer, F. Vidal, Jean Eudes Duvauchelle, Catherine Gourdon, L. Thevenard

Origin of low-field microwave absorption in metallic magnetic films evidenced in FeRh/Ta/GaAs

D. Nguyen Ba,[1] G. Olivetti,[1] T. Tremblais,[1] I. Boventer,[2] F. Vidal,[1] J.-E. Duvauchelle,[1] C. Gourdon,[1] and L. Thevenard[1]

[1]*Sorbonne Université, CNRS, Institut des Nanosciences de Paris, 4 place Jussieu, 75252 Paris, France*
[2]*Laboratoire Albert Fert, Université Paris-Saclay, 91767, Palaiseau, France*
(*thevenard@insp.jussieu.fr)
(Dated: September 25, 2024)

Performing ferromagnetic resonance (FMR) experiments on a polycrystalline FeRh (270nm)/Ta (100nm)/GaAs film, we evidence a low-field hysteretic signal, in addition to the usual non-hysteretic FMR absorption peaks. Its coercivity coincides with the static coercivity of the sample, which can be strongly tuned with temperature, thanks to the first order nature of the antiferromagnetic to ferromagnetic transition of FeRh. The sample was made using a graded composition technique which allows to obtain the Fe/Rh stoechiometry required for the presence of an antiferromagnetic-ferromagnetic transition. We show that the low-field microwave absorption (LFMA) signal can be well modelled by simply introducing the hysteresis of the static magnetization in the dynamic magnetic susceptibility. Finally, previous observations of LFMA on a cobalt thin film are also reproduced by this model.

INTRODUCTION

Ferromagnetic resonance (FMR) is an inestimable experimental technique to probe the magnetic properties of thin films[1], be it their magnetic anisotropy, gyromagnetic ratio, intrinsic and extrinsic damping or exchange constant. It relies on using an external radiofrequency (rf) field to set the magnetization into forced precession, and an rf power detector (typically a diode) to probe the electromagnetic losses as a function of a static magnetic field. In typical experiments, one takes care to remain outside the magnetic hysteresis range of the material. This is achieved by either working at fixed field sign, or by ramping the field *down* from the saturated state. However, intriguing hysteretic FMR signals (also known as "low-field microwave absorption", or LFMA) have been observed in various polycrystalline metallic systems [2–8], with the hysteresis occurring at fields neighbouring the DC coercivity of the samples. Despite previous attempts at interpretating this effect, in particular by correlating it to a similar low-field coercivity observed in giant magneto-impedance experiments[9], no clear model has emerged so far to explain the origins of LFMA.

In this report, we reproduce and model these observations by performing positive and negative-field swept FMR on a polycrystalline film of FeRh/Ta/GaAs. The main interest in using this material for this study lies in the convenient variation of its coercivity with temperature, which allows us to confirm unambiguously the correlation between the rf coercivity observed in the FMR experiments and the DC coercivity of the magnetization. FeRh is an antiferromagnet (AFM) which undergoes a first order phase transition to a ferromagnetic state around room-temperature. The coexistence of AFM and FM phases during this transition is responsible for the strong temperature-variation of the coercivity [10]. Although it was discovered almost 90 years ago [11], FeRh is currently generating renewed interest for spintronics thanks to its bistable AF state [12], for very fundamental studies on laser-pulse triggered phase changes[13–16] and for energy harvesting because of its sizable magnetocaloric effect [17]. Its FM magnetization dynamics are of high relevance to these studies, and have been measured by various FMR techniques[18–23]. Up to now, none of these studies had explored the low-field range necessary to evidence LFMA experimentally. We fill this gap by performing field-swept FMR at various temperatures. Clear LFMA signals are obtained up to 25 GHz. We show that taking into account the hysteresis in the usual Polder susceptibility is sufficient to reproduce the important features of our data, as well as that of previous authors[24]. This provides a definitive explanation for the up-to-now elusive origins of the LFMA phenomenon.

SAMPLE GROWTH BY GRADED COMPOSITION TECHNIQUE AND CHARACTERIZATION

FMR studies on FeRh were up to now[18–23] systematically done on thin ($\leq$90 nm) films grown over MgO. Here we grew instead a comparatively thick (270nm) film over Ta(100nm)/GaAs, by using a graded composition sputtering technique[25, 26] which we briefly describe below.

In FeRh, there is only a narrow window of element stoechiometry that allows the appearance of the AFM state[11]. This is usually achieved with an equiatomic target, or two separate Fe and Rh targets and by very regularly re-calibrating powers and gas flows, since both materials have slightly different sputter etch rates. Here instead, a Rh foil is positioned over half a Fe target, as shown in Fig. 1(a), so that different parts of the (non-rotated) sample will see different ratios of Fe and Rh during the growth. A 100 nm thick Tantalum buffer layer is first deposited to prevent intermixing of FeRh and GaAs, using an Ar pressure of 5×10^{-4} mbar and a radiofrequency (rf) power of 100 W (deposition rate of around 15 nm min^{-1}). This is followed by the growth of the 270 nm thick FeRh film at the same Ar pressure and rf power, leading to a deposition rate of 4.2 nm min^{-1}. After the growth, the ordered B2 phase is obtained by a post-growth annealing process at 823 K for 90 minutes (see Appendix).

A straightforward indication of whether the growth has been successful is a simple visual observation of the wafer: a clear demarcation line appears as the contrast changes from dark to bright when the Rh composition allows for the exis-

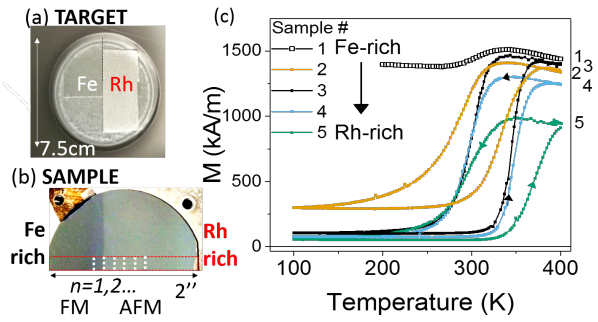

FIG. 1. Graded composition growth technique[25, 26]: (a) A piece of Rh rests on a Fe sputter target, which faces the non-rotating sample holder. (b) Sample after annealing: a reflectivity contrast clearly appears between the Fe-rich, low reflectivity FM zone and the Rh-rich high reflectivity AFM zone. (c) SQUID measurement of the magnetization versus temperature under a 50 mT in-plane field. The diamagnetic contribution of the GaAs substrate was not removed. Sample numbering refers to that of (b). The data for sample 3 is indicated by black symbols, and only the down-ramp is shown for sample 1.

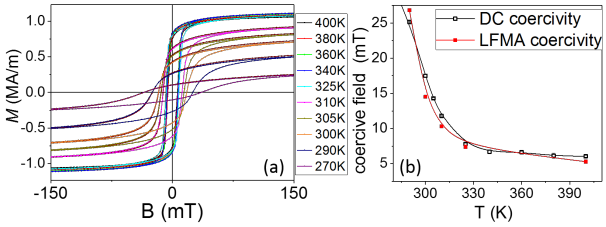

FIG. 2. VSM on the sample measured by field-modulated FMR: (a) Low-field zoom of the hysteresis cycles across the transition: the temperature is decreased down from 400 K. (b) Static (resp. LFMA) coercivity in open (resp. closed) symbols extracted from the DC hysteresis cycles of (a) (resp. the 15 GHz FMR data of Fig. 3(d)).

tence of a room-temperature AFM phase (Fig. 1(b)). FeRh is indeed known to exhibit a 3-5 % reflectivity drop upon transiting from the AFM to the FM phase[25, 27, 28]. To characterize quantitatively the magnetic behavior of the film, the central-most part of the wafer was cut into $2\times2\,\mathrm{mm}^2$ samples along the Rh concentration gradient (Fig. 1(b)). Magnetization versus temperature curves were taken using SQUID magnetometry (Fig. 1(c)). A clear evolution of the magnetic behavior is observed, from the Fe-rich sample (#1) exhibiting a very small low-temperature AFM contribution, to the optimal Rh concentration (#3), and finally the #5 Rh-rich sample exhibiting a wide transition, but low magnetization in the high-temperature FM state. In particular, sample 3 exhibits a high 400 K magnetization, and a very weak 7% residual FM phase at low temperature, similar to state-of-the art epitaxial FeRh samples[10]. The transition is however wider - around 60 K (defined as the 10-90% level of the transition) - and at lower temperatures: the warming/cooling branches are centered around 345 K/298 K. Finally, X-Ray diffraction indicated the layer to be polycrystalline (see details in the Appendix).

To summarize, this technique gives in a single growth a series of samples with varying Rh concentration among which a few will always present the right Fe/Rh stoechiometry for room-temperature AFM behavior, independently of the history of the target.

FERROMAGNETIC RESONANCE

Experimental conditions

Previous variable-temperature FMR studies on FeRh have used coplanar waveguide (CPW) or cavity geometries, varying either the frequency (at fixed field [19]), or the field (at fixed frequency [18, 21–23]). Here we use the latter approach, with an additional field-modulation to increase the signal to noise ratio [29]. A 3×5 mm² sample is cut out from the region whose Rh concentration allows an AFM↔FM transition, and its magnetic hysteresis characterized by Vibrating Sample Magnetometry at various temperatures across the transition (Fig. 2(a)). Notice that as expected for FeRh[10, 30], the static coercivity diverges when entering the AFM phase from the FM phase. This is known to originate from the decrease of available FM nucleation sites, due to the decreasing proportion of FM phase in the film[10].

The sample is then inserted in a Physical Property Measurement System (PPMS). It is installed magnetic face down onto a broadband CPW generating an rf field $\boldsymbol{h}_{CPW}$ (Fig. 3(a)). The CPW is surrounded by two small modulation coils, and the measured signal is the field-derivative of the FMR signal, dV_{FMR}/dH. The static field is applied along the sample edge (<110> axis of GaAs). The sample was brought to a FM state at 400 K, and field-modulated FMR was performed cycling the field as $B_{max} \rightarrow -B_{max} \rightarrow B_{max}$ at varying frequencies (f=0.3 to 25 GHz). The procedure was repeated at decreasing temperatures until reaching the AFM state.

We plot in Fig. 3(b-d) the component of the signal that is in-phase with the modulation field, dV_X/dH. Two features can clearly be identified, which both disappear when entering the AFM phase: a clear, non-hysteretic (FMR) signal at high field (150 mT for instance in the 400 K, 15 GHz data of Fig. 3(d)), and a low field, hysteretic one (zoom in Fig. 3(e)). We detail each of these contributions below.

Resonance fields, and gyromagnetic ratio

The FMR signal is unipolar, quite far from the expected bipolar Lorentzian-derivative shape. This can be accounted for by the Oersted field $\boldsymbol{h}_{eddy}$ generated by eddy currents I_{eddy} created in the sample by the time-varying rf field [31, 32]. The total field seen by the ferromagnetic film is then $\boldsymbol{h}_{rf}(t)=\boldsymbol{h}_{CPW}(t)+\boldsymbol{h}_{eddy}(t)$. The fairly resistive nature of FeRh yields an electromagnetic skin depth between 2 and 10 μm at our working frequencies: $\delta(B)=\sqrt{\frac{2\rho}{\omega\mu_0\mu_r(B)}}$, μ_r being the magnetic permeability[33], $\omega=2\pi f$ the angular rf frequency,

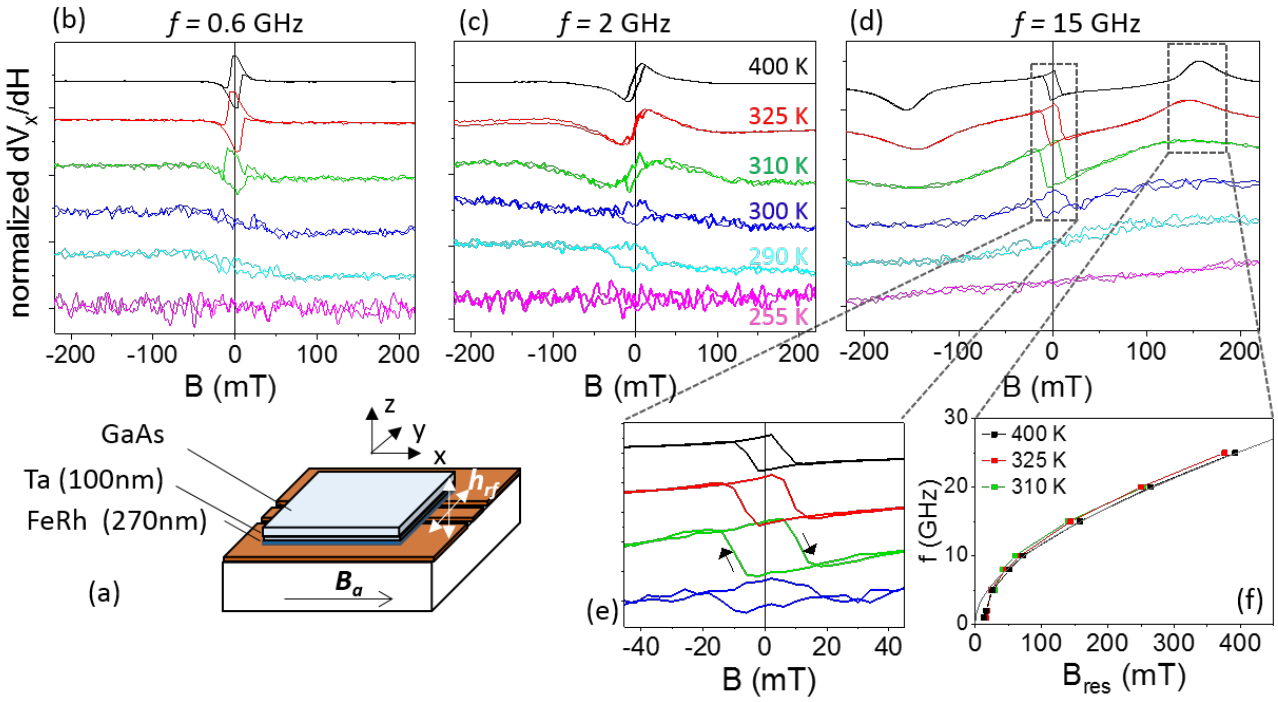

FIG. 3. Temperature-dependent field-modulated FMR experiment at different rf frequencies: (a) Schematics of the set-up and sample. (b)-(d) Normalized field scans of the derivative of the FMR signal. (e) Zoom on the low-field microwave absorption occurring in the FM phase at varying temperatures, f=15 GHz. (f) Excitation frequency versus resonance field at temperatures exhibiting an appreciable proportion of FM phase. The continuous line is a high-field fit to Eq. 1. yielding a gyromagnetic ratio of $\gamma = 1.82\times10^{11} \pm 0.01$ rad s^{-1} T^{-1}.

and ρ the resistivity of the film[34]. The rf field therefore penetrates deep into the FeRh film and the Ta film with five times higher conductivity. As described at length by Flovik *et al.*[31] and Gladii *et al.*[32], in the ideal case of zero inductance in the film where the eddy currents are created, the phase lag between $\boldsymbol{h}_{eddy}$ and $\boldsymbol{h}_{CPW}$ is exactly 90° (since $I_{eddy} \propto \frac{\partial h_{rf}}{\partial t} = i\omega h_{rf}$). In reality, the inductance and resistance of the conducting films (here FeRh and Ta) induce an additional phase shift ϕ as follows: $\boldsymbol{h}_{rf}(t) = \boldsymbol{h}_{CPW}e^{i\omega t} + \boldsymbol{h}_{eddy}e^{i(\omega t-\phi)}$. This dephasing has been shown to distort FMR lineshapes from Lorentzian derivatives to lineshapes even with respect to the resonance field [31, 32]. We further adopt the notation of Flovik *et al.*[31] who introduce the alternative parameters β_y, β_z and effective rf field $\boldsymbol{h}$ to express the in-plane and out-of-plane components of the total rf field: $h_{rf,y}$=$h_y(1-i\beta_y)$ and $h_{rf,z}$=$h_z(1-i\beta_z)$. β_y, β_z are directly related to the phase ϕ, and have been found [31, 32, 35] between -2.8 and +70.

The resonance field was thus taken at the maximum of the FMR signal and plotted versus the frequency at different temperatures (Fig. 3(f)). At low frequencies, this FMR peak merges with the low-field, hysteretic signal, preventing precise pointing of the resonance. As seen by previous authors, when the temperature decreases, the area under the FMR curve decreases and the linewidth broadens while the resonance field for a given frequency varies weakly. This is expected[22, 36] from the decrease of the total moment of the film upon nucleation of the AFM phase, while the anisotropy constants and saturation magnetization M_s of the FM fraction governing the resonance position vary weakly in this temperature range. The high-field part of the $f(B_{res})$ data is fitted by the Kittel equation giving the resonance frequency (or Eq. 1, with $m_{0,x}$=1 , B_a the applied field, and the uniaxial anisotropy field B_u taken here as null) taking M_s=1101 kA m^{-1} from the VSM data of Fig. 2(a).

$$\omega_0 = \gamma\sqrt{[m_{0,x}(\mu_0 M_s + B_u) + B_a]\,[B_a + B_u m_{x,0}]} \qquad (1)$$

This yields a gyromagnetic ratio $\gamma = 1.82\times10^{11} \pm 0.01$ rad s^{-1} T^{-1}, *i.e.* a g-factor of 2.07± 0.01, in agreement with the g=2.05± 0.06 value found by Mancini *et al.*[22]. Finally we note that the resonance linewidth increases non-linearly with frequency, with a strong zero-field intercept. This points to a large inhomogeneous broadening, compatible with the polycristalline nature of the film. We believe a precise determination of α by fitting the FMR linewidth with respect to frequency is not relevant here, given the the strong mixing of real and imaginary parts of the susceptibility.

Low field microwave absorption

Fig. 3 (and in particular the low-field zoom in (e)) shows the first evidence of a hysteretic FMR (LFMA) signal in FeRh. LFMA had been seen before up to 9.5 GHz on other polycrystalline ferromagnetic metals such as cobalt [24], FeSi [4],

NiMnSn [3], FeBN and FeCoSiB [2, 5] or ferrites[7], but never up to such high frequencies as 25 GHz. The quantitative analysis of this feature is complicated at the lower frequencies for which it distorts the incoming FMR signal, eventually completely merging with it at around 2 GHz. Therefore, we focus for the discussion on frequencies above 8 GHz.

The coercivity of this signal, which will be called "LFMA coercivity" , does not vary significantly with rf frequency, but increases as the temperature decreases and the AFM fraction grows. Fig. 2(b) shows for f = 15 GHz that this coercivity is nearly identical to the *static* coercivity of the sample[37] This is compatible with the previous observations of Modak *et al.*[3] who evidenced a very close correspondance between LFMA and static coercivities. In this case, the coercive field was varied by applying the field at different angles from a uniaxial anisotropy axis. One also notices that for frequencies allowing the two contributions to be well separated, the ratio of the peak-to-peak amplitude of LFMA and FMR signals (taken respectively at B_a=0 and B_{res}) decreases with increasing frequency (by a factor of two in the studied range, Fig. 5(a)). Again, a similar observation had been made by Lee *et al.*[24] on cobalt up to 5 GHz. In order to explain our data, we now propose a simple macrospin model capable of reproducing these features, as well as observations made by previous authors.

FMR MODEL CAPABLE OF RENDERING LFMA

Magnetization dynamics equations

We model the magnetization dynamics in the usual way by linearizing the Landau-Lishitz-Gilbert equation as a function of the normalized magnetization components, $\boldsymbol{m}$=$\boldsymbol{M}$/M_s. We assume small variations of the magnetization $\boldsymbol{\delta m}(t)$, around an equilibrium $\boldsymbol{m_0}$ driven by small variations $\mu_0\boldsymbol{\delta H}_{\rm eff}(t)$ of the effective field around $\mu_0\boldsymbol{H}_{\rm eff,0}$, and a damping α, reflecting both intrinsic and extrinsic sources of damping. The effective field and its derivative are given by the gradient of the magnetic energy, $\mu_0\boldsymbol{H}_{\rm eff}$ = -$\nabla_{\boldsymbol{M}}E$, with:

$$\frac{d\boldsymbol{\delta m}}{dt} = -\gamma(\boldsymbol{m}_0 \times \mu_0\boldsymbol{\delta H}_{\rm eff} + \boldsymbol{\delta m} \times \mu_0\boldsymbol{H}_{\rm eff,0}) + \alpha\boldsymbol{m}_0 \times \frac{d\boldsymbol{\delta m}}{dt} \quad (2)$$

$$E = -\mu_0\boldsymbol{M}\cdot\left(\boldsymbol{H}_a + \boldsymbol{h}_{rf}(t)\right) + \frac{\mu_0 M_s^2}{2}m_z^2 - K_u m_x^2, \quad (3)$$

The static field $\boldsymbol{B_a} = \mu_0\boldsymbol{H_a}$ is applied along the x direction. The total rf field $\boldsymbol{h}_{rf}$ is expressed as detailed above using $\beta_{y/z}$ and $\boldsymbol{h}$. K_u is an x-axis uniaxial anisotropy term used to model the coercivity of the layer, with the hysteresis occurring in a Stoner-Wohlfarth macro-spin switching model at B_c=B_u=$\frac{2K_u}{M_s}$. This choice will discussed further on. Searching for solutions of the type $\delta m_{y/z}(t)$=$\delta m_{y0,z0}e^{i\omega t}$ upon solving Eq. (3) leads to a 2×2 determinant from which are derived in a standard way the Polder susceptibility tensor $\boldsymbol{\delta m}$=$[\chi_P]\mu_0\mathbf{h}$ (Eq. 4), and the magnetic eigenfrequency ω_0=$2\pi f_0$ (Eq. 1):

$$\begin{cases} [\chi_P] &= \frac{1}{D}\begin{bmatrix} \frac{m_{0,x}B_a+B_u+\frac{\alpha i\omega}{\gamma}}{(1-\beta_y i)} & \frac{i\omega}{\gamma m_{0,x}(1-\beta_z i)} \\ -\frac{i\omega}{\gamma m_{0,x}(1-\beta_y i)} & \frac{\mu_0 M_s+B_u+m_{0,x}B_a+\frac{\alpha i\omega}{\gamma}}{(1-\beta_z i)} \end{bmatrix} \\ D = & \frac{\omega_0^2-(1+\alpha^2)\omega^2-\alpha\gamma B_\alpha i\omega}{\gamma^2(1-\beta_y i)(1-\beta_z i)} \\ B_\alpha &= \mu_0 M_s + 2B_u + 2B_a m_{x,0} \end{cases} \quad (4)$$

In these expressions, instead of assuming as usual $m_{x,0}$ = +1 (resp. $m_{x,0}$ = -1) for B_a>0 (resp. B_a<0), we take the explicit hysteretic field-dependence of the static magnetization $m_{x,0}$. To begin with, we take a square $m_{x,0}(B_a)$ loop crossing zero at B_c=$\frac{2K_u}{M_s}$, with M_s=1101 kA/m from the magnetometry data (Fig. 2(a)) and K_u=3250 J/m^3 taken to reproduce the experimentally observed high-temperature 5.9 mT coercive field (Fig. 2). In Fig. 4(a) we plot the eigenfrequency given by Eq. (1), using the gyromagnetic ratio value γ=1.82×10^{11} rad s^{-1} T^{-1} determined experimentally above. Because of the magnetic hysteresis, it is naturally also hysteretic. Allowing field and magnetization to be antialigned over a small field range moreover results in the eigenfrequency dropping to zero at $|B_a|$ = B_c (see inset of Fig. 4(a)). The power absorbed by the magnetic system is given by P_{abs}=$-\frac{1}{2}\Re\int_{V_{mag}} i\omega([\chi_P]\mu_0\boldsymbol{h}_{rf}).\mu_0\boldsymbol{h}_{rf}^{\dagger}dV$, where V_{mag} is the ferromagnetic volume exposed to the CPW field. In field-modulated FMR, the detected signal is proportional to the field-derivative of P_{abs}, i.e. to the derivative of the imaginary part of the diagonal components of $[\chi_P]$ (Eq. 5, in which the double-prime indicates the imaginary part).

$$\frac{dP_{abs}}{dH} = -V_{mag}\frac{\omega}{2}\left(\frac{\partial\chi''_{yy}}{\partial H}|\mu_0 h_{rf,y}|^2 + \frac{\partial\chi''_{zz}}{\partial H}|\mu_0 h_{rf,z}|^2\right) \quad (5)$$

Modelling hysteretic FMR

We then plot the absorbed power (Fig. 4(b)) and its field-derivative (Fig. 4(c)) taking into account the static hysteresis in the Polder tensor. As highlighted in the low-field zooms of the figure insets, the positive (resp. negative) slope for up (resp. down) field ramp direction in $P_{abs}(H)$ naturally give an up (resp. down) level in d$P_{abs}(H)/dH$, and the opening of a small hysteresis cycle.

The 400 K hysteresis cycle measured on the FM-FMR sample does not switch abruptly (Fig. 2(a)). There is a slight slope, likely due to a dispersion of one of the magnetic parameters, the most probable being the saturation magnetization, M_s. This could result from a slight Rh gradient across the sample, which will translate into a spread of the saturation magnetization at a given temperature (see for instance the variation of M_s(400 K) with Rh content in Fig. 1(c)). A final refinement in the modelling involves including this experimental dispersion of the coercivity through that of M_s. Modelling it as a Gaussian distribution around a central value $< M_s >$, $P(M_s)$=$\frac{1}{\sqrt{2\pi}\sigma_{M_s}}\exp\left(-\frac{(M_s-<M_s>)^2}{2\sigma_{M_s}^2}\right)$, we

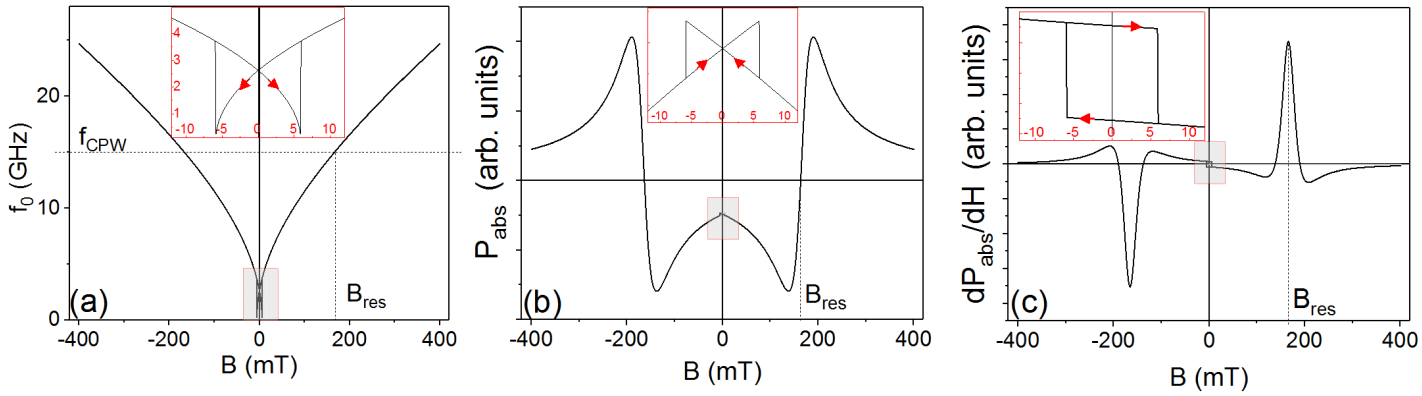

FIG. 4. Different steps in the modelling of the field-modulated FMR response, assuming here no dispersion on the saturation magnetization, β_y=β_z=10, $\mu_0 h_y$=$\mu_0 h_z$=0.1 mT, and f=15 GHz. Red arrows indicate the field ramp direction, and insets show a ±12 mT zoom of each plot. (a) Eigenfrequency calculated using Eq. 1. (b) Absorbed power. Note the Lorentzian derivative shape given by the eddy-current induced mixing of reactive and dissipative parts. (c) Field-derivative of the absorbed power to which the measured signal is proportional, calculated using Eq. 5.

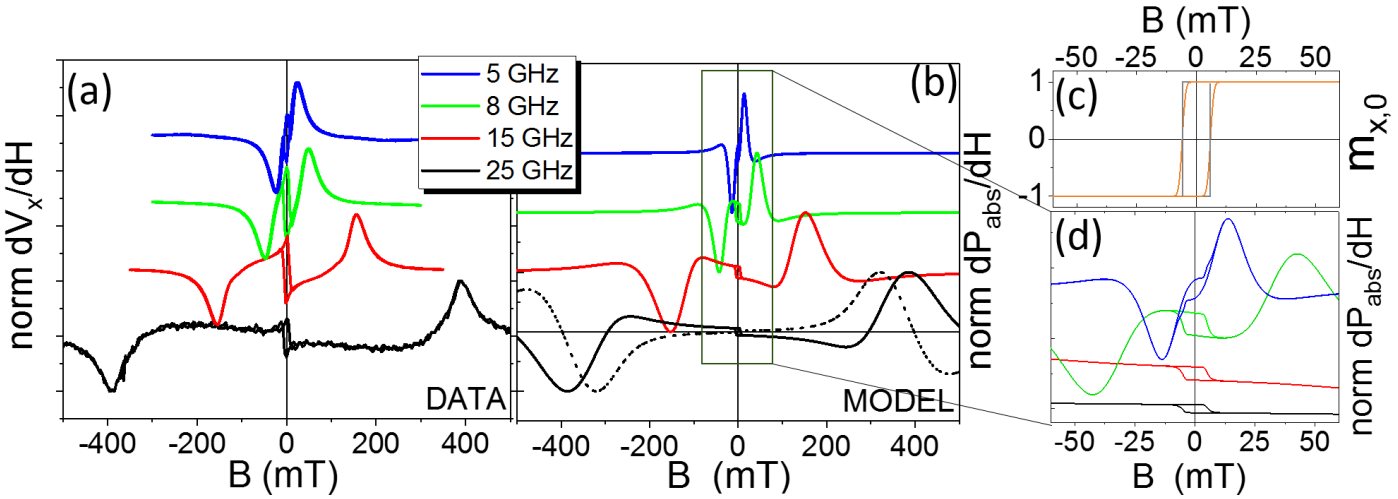

FIG. 5. Frequency-dependence of FMR data and modelling : (a) Data at different frequencies, normalized to the maximum value (T = 400 K). (b) FMR signal calculated using Eq. 5 weighted by a Gaussian distribution (σ_{M_s}=300 kA m^{-1}), normalized to the maximum value. $\mu_0 h_y$=$\mu_0 h_z$=0.1 mT and β=10 for all curves except the dashed one for which β=0. (c) Modelling of the hysteresis of the static magnetization entering Eqs. 4 without (black line), or with (orange line) dispersion on M_s - normalized cycles. (d) Low-field zoom of the calculated FMR plots of (b).

can for instance compute the normalized average $m_{x,0}(B)$ cycle (Fig. 5(c), orange plot). The expected FM-FMR signal is then calculated by weighting Eq. 5 with this distribution: $\frac{1}{N_{M_s}} \sum_{i=1}^{N_{M_s}} P(M_{s,i}) \frac{dP_{abs}}{dH}(M_{s,i})$. To begin with we set $\mu_0 h_y$=$\mu_0 h_z$=0.1 mT and β_y=β_z=β=10. We need an effective damping parameter of α=0.05 to reproduce the lineshapes, compatible with previous estimates of the effective damping (e.g. α=0.076 found by Heidarian *et al.* [21]). The results for different rf frequencies (f = 5, 8, 15 or 25 GHz) and T = 400 K are shown in Fig. 5(b), normalized to their maximum value.

Discussion

The main features of the data are now compared to those of the model, plotted using identical colors in Fig. 5(a), and also normalized to the maximal value.

Firstly, the model replicates the central, hysteretic absorption. This hysteresis reflects the dependency of the magnetic susceptibility and eigenfrequency on the static magnetization orientation, $m_{x,0}(B)$ (Eqs. 3, 4, and Fig. 4(a)). The sharpness of the low-field hysteresic switch is directly related to the dispersion of coercivity introduced by that of M_s. The FMR peak eventually merges with this signal at low frequency (f=5 GHz for instance, as shown in the low-field zoom of Fig. 5(d)).

Secondly, the increasing relative importance of the LFMA signal with respect to the FMR peak as the rf frequency is lowered is also reproduced: this model shows it is roughly multiplied by two when the rf frequency is divided by three, as observed experimentally (Fig. 5(b)). At fixed frequency, we find the calculated LFMA/FMR ratio to increase with both the damping α and the dispersion σ_{M_s}. This clearly appears when comparing σ_{M_s}=0 and 300 kA m^{-1} calculated FMR signals for f=15 GHz (Figs. 4c and 5b,d) . α and σ_{M_s} will indeed both decrease the amplitude of the FMR signal by broadening it, while weakly affecting the LFMA signal. Reproducing both the experimental lineshapes and LFMA/FMR ratio therefore results from a subtle interplay between these parameters. We obtain in the end an underestimation of this ratio, by a factor of about 3.2±0.2 at 8 GHz for instance.

Thirdly, the unipolar FMR lineshape is reproduced via the β parameter, which conveys the presence of dephased eddy-currents fields, as already evidenced by Flovik and Gladii *et al.*[31, 32]. This clearly shows up when computing β=0 and β=10 plots for a set frequency (*e.g.* f=25 GHz in full and dotted lines in Fig. 5(b)). Whether using cavity FMR[18, 21] or CPW-FMR[19, 22], previous resonance data on FeRh has consistently been taken on fairly thin films (30 to 90 nm) grown over insulating substrates. Here instead, the thick metallic FeRh layer on-top of the 100 nm-thick metallic tantalum are the source of strong eddy-current fields. Increasing β gradually deforms the lineshape from fully bipolar (β=0) to unipolar ($\beta \geq$10). Pushing β above 10 does not induce any further modification to the lineshape, but only modifies the absolute amplitude of the signal. Finally, we note that the relative weight of b_y to b_z effective rf field components, and β_y to β_z dephasing parameters influences very little the lineshape and relative amplitude of the LFMA and FMR signals. Their value is however bound to depend critically on the geometry of the sample and its positioning on the CPW.

As detailed above, this simple macrospin model reproduces accurately the main features of the data. We now confront it to previous approaches used to describe the hysteretic LFMA observed in amorphous materials[3–5, 7–9, 24, 38]. It has in particular been suggested that LFMA and low-field giant magneto-impedance (GMI) reflect identical processes of electromagnetic absorption[5, 9, 38, 39], since coercivity was found to appear at similar fields in both types of experiments[3, 9]. In the case of GMI, an rf current is made to go *through* the sample and its complex impedance measured as a function of the field. For *conductive* magnetic samples, both microwave absorption and impedance measurements are often analyzed in terms of the AC surface impedance $Z_s = \frac{E_s}{H_s}$ given by the ratio of the surface magnetic and electric fields[5]. The field-derivative of the absorbed power is then expressed as $\frac{dP_s}{dH} = \frac{H_s^2}{2}\frac{d\Re(Z_s)}{dH}$ with [8] $Z_s \propto \frac{(1+i)\rho}{\delta}$. Any hysteresis in the static magnetization will thus reflect onto the penetration depth of the AC current or field, $\delta(B)=\sqrt{\frac{2\rho}{\omega\mu_0\mu_r(B)}}$ via the magnetic permeability. Beyond this general framework, there has been no specific analytical model describing the role of hysteresis in LFMA and GMI experiments. One approach however focuses on the role of *domain walls* which appear at the coercive field. Machado *et al.*[8, 38] studied their contribution to $\delta(B)$ in the particular geometry of magnetic ribbons hosting alternating $\uparrow$ / $\downarrow$ domains along a transverse easy axis. The magnetic permeability was taken as $\mu=\mu_0(1+\chi_P(B)+\chi_{DW}(B))$, sum of the non-hysteretic Polder susceptibility χ_P, and a lower-frequency susceptibility due to the damped breathing of domain-walls, χ_{DW}. Introducing this term in the surface magnetoimpedance via $\delta(B)$ reproduced with success the frequency dependence of the GMI amplitude of $Co_{70.4}Fe_{4.6}Si_{15}B_{10}$ ribbons[38]. The contribution of the domain-walls was found to vanish at around 1 MHz, which makes this effect unlikely to be at play in our high frequency LFMA signal, in addition to the fact that the magnetic geometry of Machado's model is very different from ours.

Lee *et al.* [24] suggested instead, without modelling it, that these features could stem from the scattering of the FMR mode with magnetic inhomogeneities of the multi-domain state, a hypothesis compatible with GHz excitation frequencies. In their work on a thin cobalt film, FMR data quite similar to that of Fig. 5(a) was obtained, with a high-field, non-hysteretic FMR signal coexisting with a low-field hysteretic opening. Focusing on their f=5 GHz curve in which both signals are well separated, we show in Fig. 6 that their data can be reproduced quite well using the hysteretic FMR model presented above, without introducing any scattering effects. For this Eq. 5 was used to calculate the expected field derivative of the absorbed power, with $\mu_0 h_y$=$\mu_0 h_z$=0.1 mT and their experimental magnetic parameters. A dephasing term $\beta_y = \beta_z$ = -0.6 was necessary to obtain their slightly asymmetric FMR lineshapes. A depinning field of B_{dep} = 2.2 mT (0.7B_u with B_u = 3.4 mT given by Lee *et al.* [24]) and σ_{M_s}=100 kA/m were used to reproduce at best the hysteresis. The shape of the data is overall very well reproduced. The ratio of LFMA to FMR contribution is slightly underestimated, as in Fig. 5(b) for FeRh. Overall however, this comparison shows that, despite its simplicity, a macrospin hysteretic FMR model is a viable route to explain the hysteretic LFMA part of the FMR data of Lee *et al.* as well, contributing consistently to the overall picture of the phenomenon.

We now discuss two strong hypotheses of this model: (i) that of a macrospin switching, (ii) that of a uniaxial anisotropy in Eq. 3. As illustrated in Fig. 4, what is necessary for LFMA to appear is essentially a hysteresis in the magnetic eigenfrequency, which results from a hysteresis of the magnetization, i.e. the possibility for applied field and magnetization *not* to lie parallel over a particular field-range (see Eq. 1). In order to use a very simple macrospin framework in which to express the magnetization dynamics, a unixial anisotropy term was introduced, but we could equally have taken a cubic anisotropy, an isotropic depinning term or any combination of anisotropies term giving an open hysteresis loop. Naturally, the large magnetic volume implies that switching will probably occur at a fraction of the macrospin switching field by domain nucleation/propagation. This will simply imply modelling the hysteresis of $m_{0,x}$ with the experimentally observed coercive field, as done when interpreting the LFMA data of Lee *et al.* (switching field B_c taken as 0.7B_u, see above and Fig. 6). We note finally, that while it is very unlikely that

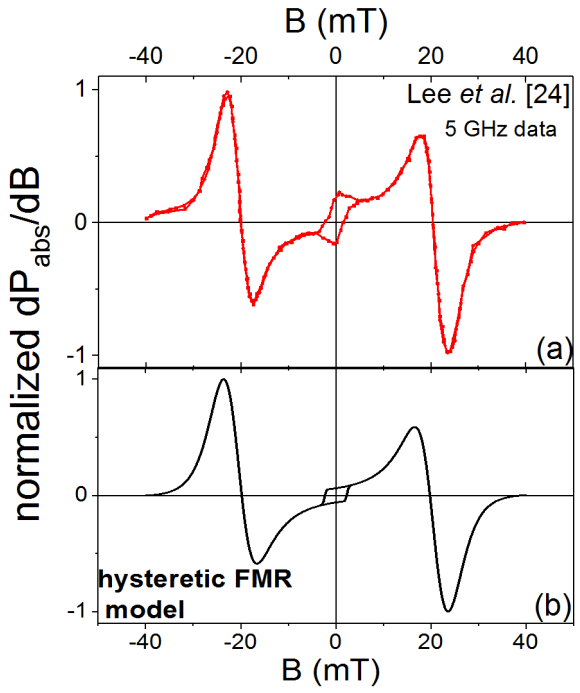

FIG. 6. Using the hysteretic FMR model presented in this work to reproduce the hysteresis in the FMR data of Lee *et al.*[24], taken on a 40 nm-thick cobalt film sputtered on a Si substrate. (a) f=5 GHz curve (adapted from Fig. 3 of Ref. 24). (b) FMR signal calculated using Eq. 5, magnetic parameters γ, M_s, K_u and α taken from Ref. 24, and $b_y = b_z$=0.1 mT, $\beta_y = \beta_z$=-0.6, and σ_{M_s}=100 kA/m. Both curves are normalized between -1 and +1.

domain-wall resonance could intervene in LFMA, taking into account the presence of multiple magnetic domains might allow a better description of the LFMA/FMR ratio, a value that is slightly underestimated in the current model.

CONCLUSIONS

In this study we report the successful growth of FeRh over GaAs. Although the piezoelectric nature of this substrate did not play any role in the observation of LFMA, it presents the broader interest of allowing the straightforward implementation of an electrical control of the magnetic properties of FeRh via its magnetoelasticities[40]. This moderately piezoelectric but non ferroelectric material is indeed an interesting alternative to the brittle and pricy PMN-PT (lead magnesium niobate-lead titanate), or multi-ferro-electric-domain $BaTiO_3$ substrates currently used for the electric-field tuning of the magnetic properties of FeRh[41–43].

We moreover performed field-modulated FMR experiments on polycristalline FeRh films. Unipolar non-hysteretic FMR peaks were observed, for which the shape likely derives from the presence of the large metallic volume (thick Tantalum and FeRh layers), inducing substantial eddy currents. More notably, we evidenced like previous authors[2–5, 7, 8] on various polycristalline ferromagnets a hysteretic low-field microwave absorption. The rf coercivity matched perfectly the DC coercivity of the sample, a correlation that was made possible to observe thanks to the strong temperature-dependence of the coercivity of FeRh, with a lesser variation of other parameters such as the saturation magnetization or anisotropy. This effect was modelled by including the hysteresis of the magnetization in the susceptibility tensor. The newly gained knowledge on the underlying origin of this effect - often considered spurious and discarded - should enable low-frequency FMR experiments to be performed in clearer conditions.

ACKNOWLEDGMENTS

This work has been partly supported by the French Agence Nationale de la Recherche (ANR ACAF 20-CE30-0027). We acknowledge M. Vabre and S. Chenot (Institut des Nanosciences de Paris) for technical assistance, D. Hrabovsky (MPBT - Mesures Physiques à Basses Températures-Physical Properties Low-Temperature Facility of Sorbonne University) for help with the magnetometry experiments, and Y. Zheng and M. Marangolo (Institut des Nanosciences de Paris) as well as M. Anane (Laboratoire Albert Fert) for fruitful discussions.

APPENDIX : DETAILS ON THE GROWTH AND STRUCTURAL CHARACTERIZATION

The graded composition FeRh growth approach presented here on 2" GaAs(001) substrates was also realized successfully on Si, PMN-PT and PZT substrates by some of the authors[25], and for FePt by Hong *et al.*[26]. As explained in the main text, it relies on exposing the substrate to a $25\times50\,\mathrm{mm}^2$ Rh foil positioned over half of a 75 mm diameter Fe target. The final Fe/Rh gradient depends finely on the target-to-sample holder distance. For example, when it is around 50 mm, a gradient of $\approx$ 5.4 at. % of Rh per centimeter in the direction normal to the Fe/Rh foil interface was measured by Energy-dispersive X-ray spectroscopy (EDXS) on a sample grown by the same method on a silicon substrate[25]. There is a strong lattice mismatch between FeRh ($\sim$2.9930Å), Ta ($a \approx 3.3029$Å[]) and GaAs ($a \approx 5.65325$ Å), so no epitaxial growth can be expected in this stack.

The structural characterizations of the annealed FeRh films were performed by high resolution x-ray $\theta - 2\theta$ scans, using a 5-circle diffractometer (Rigaku SmartLab) with Cu Kα_1 radiation ($\lambda \approx 1.540593$Å) coming from a rotating anode and extracted by a channel-cut Ge(220) 2-reflection monochromator. The X-ray spot size on the wafer was approximately 2.5 mm in length and 5 mm in width.

The X-ray out-of-plane diffraction (XRD) pattern obtained for the wafer presented in Fig. 1 is shown in Fig. 7. It clearly shows peaks corresponding to the FeRh film (in magenta and yellow), the GaAs substrate (in black) and the Tantalum buffer layer. The large peak directly at the left of the GaAs (200) is believed to come from a reaction of the Tantalum buffer layer

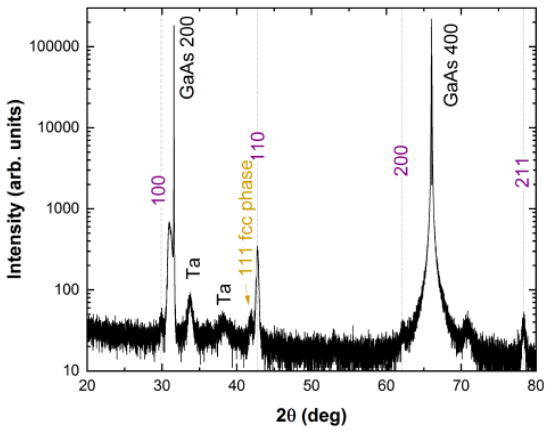

FIG. 7. XRD pattern of the sample of Fig. 1. The different FeRh phases are indicated in magenta (B2) and yellow (fcc).

with the GaAs substrate during the annealing process as this peak is also observed for samples where only the Tantalum layer was deposited. The (400) peak of an epitaxied TaAs compound is a possibility for explaining such emergence. It should be noted that the Tantalum buffer layer grown on GaAs is in the tetragonal β phase.

The different FeRh phases are indicated in magenta (B2 phase) and yellow (fcc). The appearance of the FeRh (100) peak in all measurements confirmed the formation of the B2 phase in all of our FeRh/Ta/GaAs samples. We estimated the lattice parameter of the FeRh B2 phase as $a \approx 2.9906$Å, which is in a good agreement with the value of the B2 phase of bulk FeRh[] ($\sim$2.9930Å). In short, the XRD patterns of the FeRh films suggest a good quality film, in line with the observed ferromagnetic-antiferromagnetic transition in the magnetic measurement (Fig. 1(c)). Finally, the in-plane and out-of-plane rocking curve measurements confirmed that the FeRh is polycristalline with no specific texture.

[1] M. Farle, Reports on Progress in Physics **61**, 755 (1998).

[2] J. Lee, J. Kim, and K. H. Kim, physica status solidi (a) **211**, 1900 (2014).

[3] R. Modak, A. Srinivasan, and V. V. Srinivasu, Materials Research Bulletin **143**, 111453 (2021).

[4] H. Gavi, B. D. Ngom, A. C. Beye, A. M. Strydom, V. V. Srinivasu, M. Chaker, and N. Manyala, Journal of Magnetism and Magnetic Materials **324**, 1172 (2012).

[5] G. Alvarez, H. Montiel, D. de Cos, R. Zamorano, A. García-Arribas, J. Barandiaran, and R. Valenzuela, Journal of Non-Crystalline Solids **353**, 902 (2007).

[6] G. Alvarez, H. Montiel, J. F. Barron, M. P. Gutierrez, and R. Zamorano, Journal of Magnetism and Magnetic Materials **322**, 348 (2010).

[7] R. Valenzuela, G. Alvarez, H. Montiel, M. P. Gutiérrez, M. E. Mata-Zamora, F. Barrón, A. Y. Sánchez, I. Betancourt, and R. Zamorano, Journal of Magnetism and Magnetic Materials **320**, 1961 (2008).

[8] F. L. A. Machado and S. M. Rezende, Journal of Applied Physics **79**, 6558 (1996).

[9] H. Montiel, G. Alvarez, I. Betancourt, R. Zamorano, and R. Valenzuela, Applied Physics Letters **86**, 1 (2005).

[10] J. A. Arregi, M. Horký, K. Fabianová, R. Tolley, E. E. Fullerton, and V. Uhlíř, Journal of Physics D: Applied Physics **51**, 105001 (2018).

[11] M. Fallot, Annales de physique **11**, 291 (1938).

[12] X. Marti, I. Fina, C. Frontera, J. Liu, P. Wadley, Q. He, R. J. Paull, J. D. Clarkson, J. Kudrnovský, I. Turek, J. Kuneš, D. Yi, J.-H. Chu, C. T. Nelson, L. You, E. Arenholz, S. Salahuddin, J. Fontcuberta, T. Jungwirth, and R. Ramesh, Nature Materials **13**, 367 (2014), arXiv:0402594v3 [arXiv:cond-mat].

[13] B. Bergman, G. Ju, J. Hohlfeld, R. J. Van De Veerdonk, J. Y. Kim, X. Wu, D. Weller, and B. Koopmans, Physical Review B - Condensed Matter and Materials Physics **73**, 1 (2006).

[14] M. Mattern, J. Jarecki, J. A. Arregi, V. Uhlíř, M. Rössle, and M. Bargheer, APL Materials **12** (2024), 10.1063/5.0206095.

[15] F. Pressacco, V. Uhlíř, M. Gatti, A. Nicolaou, A. Bendounan, J. A. Arregi, S. K. Patel, E. E. Fullerton, D. Krizmancic, and F. Sirotti, Structural Dynamics **5**, 1 (2018), arXiv:1803.00780.

[16] J.-U. Thiele, M. Buess, and C. H. Back, Applied Physics Letters **85**, 2857 (2004).

[17] S. Cervera, M. Trassinelli, M. Marangolo, C. Carrétéro, V. Garcia, S. Hidki, E. Jacquet, E. Lamour, A. Lévy, S. Macé, C. Prigent, J. P. Rozet, S. Steydli, and D. Vernhet, Physical Review Materials **1**, 065402 (2017).

[18] G. Kumar, S. M. Mahajan, H. A. Stretz, and S. K. Apte, Optical Materials Express **2**, 864 (2012).

[19] T. Usami, I. Suzuki, M. Itoh, and T. Taniyama, Applied Physics Letters **108** (2016), 10.1063/1.4953464, arXiv:1605.03798.

[20] T. Usami, M. Itoh, and T. Taniyama, AIP Advances **11**, 1 (2021).

[21] A. Heidarian, S. Stienen, A. Semisalova, Y. Yuan, E. Josten, R. Hübner, S. Salamon, H. Wende, R. A. Gallardo, J. Grenzer, K. Potzger, R. Bali, S. Facsko, and J. Lindner, Physica Status Solidi (B) Basic Research **254** (2017), 10.1002/pssb.201700145.

[22] E. Mancini, F. Pressacco, M. Haertinger, E. E. Fullerton, T. Suzuki, G. Woltersdorf, and C. H. Back, Journal of Physics D: Applied Physics **46**, 245302 (2013).

[23] X. Zhu, Y. Li, Y. Xie, Q. Qiu, C. Cao, X. Hu, W. Xie, T. Shang, Y. Xu, L. Sun, W. Cheng, D. Jiang, and Q. Zhan, Journal of Alloys and Compounds **917**, 165566 (2022).

[24] S. J. Lee, C. C. Tsai, H. Cho, M. Seo, T. Eom, W. Nam, Y. P. Lee, and J. B. Ketterson, Journal of Applied Physics **106**, 063922 (2009).

[25] D. N. Ba, *A study of the FM-AFM phase transition in FeRh : compositionally graded films and strain control*, Ph.D. thesis, Institut Néel (2017).

[26] Y. Hong, I. de Moraes, G. G. Eslava, S. Grenier, E. Bellet-Amalric, A. Dias, M. Bonfim, L. Ranno, T. Devillers, and N. M. Dempsey, Journal of Materials Research and Technology **18**, 1245 (2022).

[27] V. Saidl, Brajer, Vyborny, and P. Němec, New Journal of Physics **18**, 083017 (2016).

[28] S. P. Bennett, M. Currie, O. M. J. van 't Erve, and I. I. Mazin, Optical Materials Express **9**, 2870 (2019).

[29] I. Boventer, H. T. Simensen, A. Anane, M. Kläui, A. Brataas, and R. Lebrun, Physical Review Letters **126**, 187201 (2021), arXiv:2103.16872.

[30] I. Fina, A. Quintana, X. Marti, F. Sánchez, M. Foerster,

L. Aballe, J. Sort, and J. Fontcuberta, Applied Physics Letters **113** (2018), 10.1063/1.5040184.

[31] V. Flovik, F. Macià, A. D. Kent, and E. Wahlström, Journal of Applied Physics **117** (2015), 10.1063/1.4917285, arXiv:1412.1385.

[32] O. Gladii, R. L. Seeger, L. Frangou, G. Forestier, U. Ebels, S. Auffret, and V. Baltz, Applied Physics Letters **115**, 032403 (2019).

[33] M. P. Annaorazov, K. A. Asatryan, G. Myalikgulyev, S. A. Nikitin, A. M. Tishin, and A. L. Tyurin, Cryogenics **32**, 867 (1992).

[34] A. Castellano, K. Alhada-Lahbabi, J. A. Arregi, V. Uhlíř, B. Perrin, C. Gourdon, D. Fournier, M. J. Verstraete, and L. Thevenard, Physical Review Materials **8**, 084411 (2024), arXiv:hal-04531324v1.

[35] V. Flovik, B. H. Pettersen, and E. Wahlström, Journal of Applied Physics **119** (2016), 10.1063/1.4948302, arXiv:1602.07463.

[36] H. Kumar, D. R. Cornejo, S. L. Morelhao, S. Kycia, I. M. Montellano, N. R. Álvarez, G. Alejandro, and A. Butera, Journal of Applied Physics **124**, 085306 (2018).

[37] Note that the field history, ramp range and speed during the hysteresis cycles were purposefully taken identical to those used during the FMR experiments.

[38] F. L. A. Machado, A. E. De Araujo, A. A. Puça, A. R. Rodrigues, and S. M. Rezende, Physica Status Solidi (A) Applied Research **173**, 135 (1999).

[39] A. E. P. De Arauh Jo, F. L. A. Machado, F. M. De Aguiar, and S. M. Rezende, Journal of Magnetism and Magnetic Materials **226**, 724 (2001).

[40] R. Levitin and B. Ponomarev, Soviet Journal of Experimental and Theoretical Physics **23**, 984 (1966).

[41] J. D. Clarkson, I. Fina, Z. Q. Liu, Y. Lee, J. Kim, C. Frontera, K. Cordero, S. Wisotzki, F. Sanchez, J. Sort, S. L. Hsu, C. Ko, L. Aballe, M. Foerster, J. Wu, H. M. Christen, J. T. Heron, D. G. Schlom, S. Salahuddin, N. Kioussis, J. Fontcuberta, X. Marti, and R. Ramesh, Scientific Reports **7**, 15460 (2017).

[42] R. O. Cherifi, V. Ivanovskaya, L. C. Phillips, A. Zobelli, I. C. Infante, E. Jacquet, V. Garcia, S. Fusil, P. R. Briddon, N. Guiblin, A. Mougin, A. A. Ünal, F. Kronast, S. Valencia, B. Dkhil, A. Barthélémy, and M. Bibes, Nature Materials **13**, 345 (2014).

[43] Z. Feng, H. Yan, and Z. Liu, Advanced Electronic Materials **5**, 1800466 (2019).